Spectroscopy and scattering: An extended quantum defect theory for non-Rydberg resonant states

Rui Sun [1,2,3] Rui Jin [3,*] Jia-Ming Li [1,4] and Xiang Gao [3,†]

[1]*Key Laboratory for Laser Plasmas, Ministry of Education, School of Physics and Astronomy, Shanghai Jiao Tong University, Shanghai 200240, China*

[2]*Collaborative Innovation Center of IFSA, Shanghai Jiao Tong University, Shanghai 200240, China*

[3]*National Key Laboratory of Computational Physics, Institute of Applied Physics and Computational Mathematics, Beijing 100088, China*

[4]*Department of Physics and Center for Atomic and Molecular Nanosciences, Tsinghua University, Beijing 100084, China*

Non-Rydberg resonant states are a special type of resonant states with open-shell electronic configurations that cannot be partitioned into a quasi-two-body system of a tightly coupled ion target and a loosely coupled projectile electron as the case of Rydberg states, which is an important type of resonant processes in atomic and molecular systems. Previous treatments of non-Rydberg resonances in the context of multichannel quantum defect theory (MQDT) were to introduce these states as resonances in the smoothly varied MQDT parameters, and the main merit of the MQDT method for Rydberg states would be lost. To reconcile the efficiency and numerical accuracy for the calculation of non-Rydberg states, a nonperturbative calculation approach is proposed in this paper. In this approach, the smooth-varying short-range scattering matrices are obtained by applying the eigenchannel R-matrix method to the subsystem excluding the non-Rydberg states. Subsequently, the non-Rydberg states are restored using the configuration-interaction formalism. The scattering matrices with resonant structures can then be obtained directly using simple linear algebra operations. Since the ingredients of the procedure are all smooth functions of energy, only a sparse energy grid is required for the time-consuming *ab initio* calculations. This makes our method highly computationally efficient and can be considered as an extension of the traditional MQDT. To demonstrate the efficacy of our method, the resonant $e + O^+$ collisional complex in the 1^- partial wave is calculated. In addition, we demonstrate that the numerical accuracy of the scattering matrices is significantly affected by the non-Rydberg states.

I. INTRODUCTION

Atomic and molecular energy levels and the corresponding collision processes are essential physical parameters for plasma studies ranging from astrophysical plasmas [1–6] to those in fusion energy research [7–12]. However, it is extremely challenging to compile such atomic data by experimental measurements alone, so high-precision theoretical computations are indispensable to meet these needs.

Of particular interest are the resonant processes, such as autoionization [13–16], dielectronic recombination [17], and dissociative recombination [18–20]. These mechanics play a crucial role in determining the charge state equilibration, the energy-level populations, and thus the radiative spectrum of nonequilibrium plasmas [12,21]. These resonant processes can be viewed as the result of discrete levels interacting with collisional continua, known as the Fano-Feshbach resonance [13,22–24]. Nonperturbative solutions of the problem have been given, based on the multichannel scattering theory, for cases with complexity ranging from the simplest one-discrete–one-channel to general multidiscrete-multichannel cases [13,22–27]. Several numerical approaches have been developed for accurate calculations, such as the close-coupling method [28–35] and the K-matrix method based on the Lippmann-Schwinger equation [36–43].

The direct use of such methods in practical calculations would face efficiency problems, especially for energy ranges with dense autoionization resonances, since the resonant behavior requires calculations on fine energy grids. However, due to the analytic continuation of the scattering matrices, the bound states share an intimate relationship with electron-ion collision processes in the multichannel quantum defect theory (MQDT) [44–50]. Based on the MQDT, the complex multichannel interactions within the reaction zone are represented by the short-range scattering matrices (i.e., $U_{i\alpha}$ and μ_α physical parameters in the eigenchannel representation of the MQDT), which vary smoothly with energy. Various physical quantities, including those for resonant processes, can be derived using the MQDT procedure [44–50]. Therefore, instead of calculating with fine energy grids, one only needs to obtain short-range scattering matrices on a few energy grids over the energy regions of interest, either by empirically fitting the experimental spectroscopy data or by numerical calculations, which is a unique merit of this method. In this line, we have developed the R-eigen code (an eigenchannel version based on the nonrelativistic R-matrix method) and the R-R-eigen code (an eigenchannel version based on the relativistic R-matrix method) [51–58] from the earlier Breit-Pauli [59,60]

---

*Contact author: rui.jin@mpi-hd.mpg.de

†Contact author: gao_xiang@iapcm.ac.cn

and Dirac *R*-matrix codes [61–63], respectively, to directly calculate the short-range scattering matrices in both discrete and continuum energy regions. They have been successfully applied to the treatment of many atomic processes, such as electron impact excitations [51,52,56], photoionizations [53,54,57], as well as the complex autoionization resonant structures involving multiple thresholds [57,58]. A special feature of our method is that one can easily check and calibrate the accuracy of the scattering matrices using the available spectroscopic data [64], which in turn can determine the collisional calculation uncertainty [52] and improve the calculation accuracy [57].

However, due to the strong intrashell interactions, a special kind of resonant states with open-shell electronic configurations cannot be partitioned into a quasi-two-body system of a closely coupled ion target and a loosely coupled projectile electron, which is routinely done for Rydberg states. This essential difference makes these so-called interloping states [65] or valence states [66] behave very differently from regular Rydberg states in the channel and makes them difficult to describe in the traditional MQDT framework [50,65,66]. Previous treatments of such non-Rydberg resonances in the context of MQDT have been to perturbatively introduce these states into the MQDT parameters. As a result, the smoothly varying MQDT parameters become resonant, and the main advantage of the MQDT method is lost.

In this paper, we propose a nonperturbative approach to this kind of problem in the framework of MQDT. We treat this problem by first performing an eigenchannel *R*-matrix calculation of the system excluding the non-Rydberg resonant configurations to obtain smooth scattering matrix parameters on coarse energy grids. Then the non-Rydberg resonant states are restored to obtain the resonant MQDT parameters using the configuration-interaction technique similar to Fano and Feshbach [13,22–26]. Since the calculation involves only simple linear algebra operations of low-dimensional matrices, our approach takes no more significant time than solving the usual MQDT equations. Rich physical phenomena can be studied by solving the MQDT equation with the calculated scattering matrices, such as energy levels and autoionization resonances of the entire channel, as well as cross sections and rates of dynamics including photoexcitation, collisional excitation, dielectronic recombination, etc. In this respect, our method can be seen as an extension of the traditional MQDT. With the smooth-varying configuration interactions between the eigenchannels and the non-Rydberg states introduced, one can obtain all physical states including the non-Rydberg states from smooth functions of energy on a few energy grids, thus greatly saving the computational time.

For the neutral atomic oxygen system of interest here, whether it is in a bound state or an $e + O^+$ collisional complex, it serves not only as a prototypical system in investigating the electronic correlations but also as an important subject of study in fields such as astrophysics [1,2] and environmental science [67,68]. The ratio between the two transitions $^2D^o_{5/2,3/2} \rightarrow {}^4S^o_{3/2}$ for ground state O^+ is a key quantity used to diagnose the electron densities in planetary nebulas [1,2]. In the low electron density limit, the two corresponding line intensities of interest are related to electronic collisional excitation cross sections, which shows significant

discrepancies among different theoretical approaches [3–5]. The difficulty lies in the fact that a vast amount of dense resonant structures across multiple thresholds will be encountered in the calculations in addition to the possible presence of non-Rydberg resonant states. In this paper, we will demonstrate that the precision of the scattering matrix is strongly affected by non-Rydberg resonant states, thus providing valuable insights into the origin of the persistent inaccuracy in previous calculations.

The paper is organized as follows: in Sec. II, a brief description of the theory is given, including the *R-R*-eigen method, the theoretical treatment of non-Rydberg resonant states, and the MQDT theory. Section III presents the results and discussion of the present calculation. The calculated MQDT parameters, the MQDT analysis of spectroscopic phenomena, and influences of the non-Rydberg resonant states on the coupled eigenchannels are discussed in Secs. III A–III C, respectively. Finally, concluding remarks on the present paper are given in Sec. IV.

II. THEORETICAL METHOD

A. Relativistic eigenchannel *R*-matrix method

To introduce the nonperturbative approach for the non-Rydberg resonant states within the MQDT framework based on the relativistic eigenchannel *R*-matrix method (*R-R*-eigen), a brief review of *R-R*-eigen is in order; for further details, the readers can refer to our previous works [51–53,55]. The excited structure and electronic scattering of atoms can be treated in a unified manner as an (*N*+1) problem in the half-collision picture [44,49], where the *N*+1-electron complex is partitioned into a target consisting of *N* closely coupled electrons and one scattering or excited electron. All (*N*+1) wave functions belonging to the same target-electron angular coupling type form a channel. Physical states in a symmetry block (total angular momentum and parity, i.e., J^π) are then described by the combination of various coherent channels. The interaction between the excited electron and the target ion can be treated accurately by the *R-R*-eigen method [51–53,55], which is based on the Dirac *R*-matrix code [61–63]. The major difference between the *R-R*-eigen method [51–53,55] and the traditional *R*-matrix method [33,34,60] lies in the definition of channels. Additional relevant closed channels together with the so-called open channels in the traditional *R* matrix are regrouped as physical channels (ionization channel). More specifically, the physical channels are those channels with orbital energy, $\varepsilon > -q^2/l^2$ (where q and l are the charge of a long-range potential and the angular momentum, respectively). The rest of the channels (with deep negative energy) are defined as computational channels, as counterparts to the "closed channels" in the traditional *R* matrix. These are included to ensure adequate electron correlations. This allows us to extend the definition and calculation of the scattering matrix into the bound energy region, and to unify the spectroscopic phenomena in the bound energy region and scattering phenomena in the continuum region from first principles. The key physical parameters in the MQDT framework [44,45,48–50] can be obtained by diagonalizing the short-range scattering
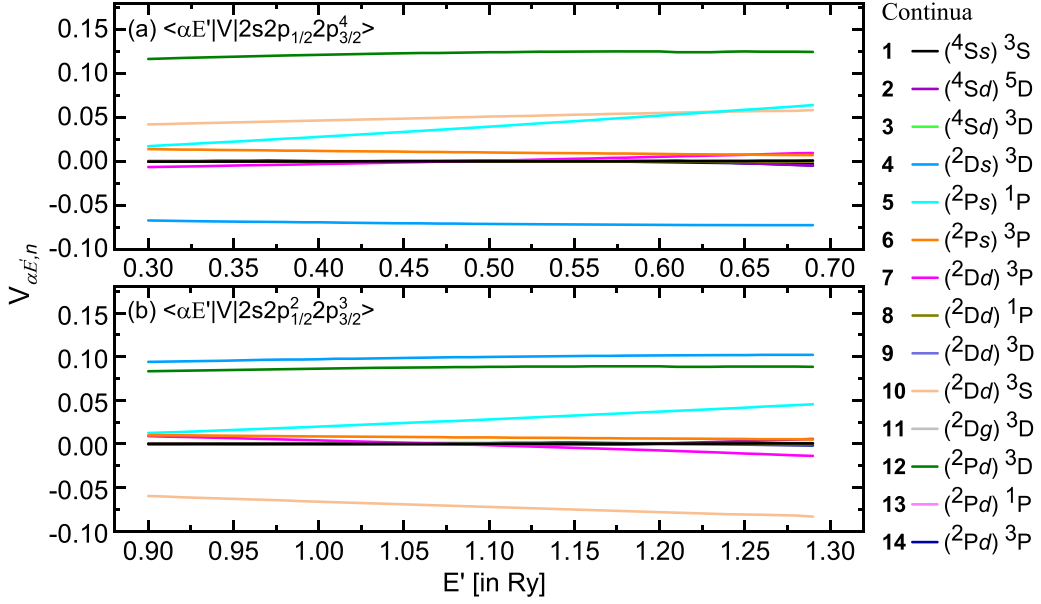
FIG. 1. Configuration-interaction terms between pure-continuum eigenchannel wave functions and two different non-Rydberg configurations $2s2p_{1/2}2p_{3/2}^4$ and $2s2p_{1/2}^2 2p_{3/2}^3$ respectively.

matrices:

$$\tilde{K}_{ij}^{J^\pi} = \sum_\alpha U_{i\alpha} \tan(\pi \mu_\alpha) U_{j\alpha}, \quad (1)$$

where μ_α are the eigenquantum defects and $U_{i\alpha}$ is the orthogonal transformation matrix. The corresponding eigenchannel wave functions Ψ_α can also be calculated using the eigenchannel R-matrix method [51–53,55]. In general, the eigenchannel scattering matrix parameters $U_{i\alpha}$ and μ_α are functions that vary slowly with energy. However, non-Rydberg resonances occur in the presence of open-shell electronic configurations, causing $U_{i\alpha}$ and μ_α to change rapidly with energy and lose the advantages of the eigenchannel method.

B. Treatment of non-Rydberg resonant states within the eigenchannel R-matrix method

The treatment of non-Rydberg resonant states within the eigenchannel R-matrix method proceeds in two steps. First, the eigenchannel wave functions without the non-Rydberg resonant states are denoted as pure-continuum type. Outside the reaction zone ($r > r_0$), these wavefunctions in terms of the unperturbed scattering matrix parameters $\{U_{i\alpha}^0, \mu_\alpha^0\}$ reads

$$\Phi_{\alpha\varepsilon}^0 = \sum_i \Theta_i U_{i\alpha}^0 \left(f_i \cos \pi \mu_\alpha^0 - g_i \sin \pi \mu_\alpha^0 \right), \quad (2)$$

with Θ_i the ionization channel function. Then the interaction with non-Rydberg resonant states is introduced using configuration-interaction formulations, similar to the procedures used by Fano and others [13,25,26], and formulated as below:

$$\langle \Phi_{\alpha\varepsilon'}^0 | \hat{H} | \Phi_{\beta\varepsilon}^0 \rangle = \varepsilon \delta(\varepsilon - \varepsilon') \delta_{\alpha\beta}, \quad (3a)$$

$$\langle \Phi_m^0 | \hat{H} | \Phi_n^0 \rangle = H_{mn}^0, \quad (3b)$$

$$\langle \Phi_{\alpha\varepsilon}^0 | \hat{H} | \Phi_n^0 \rangle = V_{\alpha\varepsilon,n}, \quad (3c)$$

where the wave functions $\Phi_{\alpha\varepsilon}^0$ and Φ_n^0 are pure-continuum eigenchannel and non-Rydberg resonant state wave functions, forming an orthogonal set:

$$\langle \Phi_m^0 | \Phi_n^0 \rangle = \delta_{mn},$$

$$\langle \Phi_m^0 | \Phi_{\alpha\varepsilon}^0 \rangle = 0. \quad (3d)$$

H_{mn}^0 and $V_{\alpha\varepsilon,n}$ are the zeroth-order Hamiltonian matrix elements between the non-Rydberg resonant states (without perturbation from the continua) and the configuration-interaction terms between the pure-continuum eigenchannel and the non-Rydberg resonant state wave functions, respectively. It is worth noting that the zeroth-order non-Rydberg resonant states shown in Eq. (3b) are not prediagonalized as done in Refs. [13,25]. The $V_{\alpha\varepsilon,n}$ is a smooth function of energy; this is the foundation of our approach to solving the problem in sparse energy grids. An illustrative example of the configuration-interaction terms is shown in Fig. 1, where two non-Rydberg resonant states are present in the O system with $J^\pi = 1^-$, i.e., $2s2p_{1/2}^2 2p_{3/2}^3$ at around 0.45 Ry and $2s2p_{1/2}2p_{3/2}^4$ at around 1.1 Ry respectively. Further details such as the designation of the channel will be introduced later in this subsection, as they are not critical for the discussion here.

The physical state at a given energy E can then be expressed as a linear combination of the pure-continuum basis and the non-Rydberg resonance states in Eq. (3d):

$$\Psi(E, i) = \sum_n A_n(E, i) \Phi_n^0 + \sum_\alpha \int_{\varepsilon_c} B_{\alpha\varepsilon}(E, i) \Phi_{\alpha\varepsilon}^0 d\varepsilon, \quad (4)$$

where the integral $\int_{\varepsilon_c}$ runs over the entire allowed energy range, i.e., from the lower limit for the eigenchannel $I_i - \frac{q^2}{l^2}$ to infinity, with I the ionization threshold and i indexes the ionization channel. Applying the unperturbed bound and continuum wave functions $\langle \Phi_m^0 |$ and $\langle \Phi_{\alpha\varepsilon}^0 |$ to the left of the

Schrödinger equation $\hat{H}\,|\Psi(E,i)\rangle = E\,|\Psi(E,i)\rangle$, we get a coupled integral equation set of the expansion coefficients $A_n(E,i)$ and $B_{\alpha\varepsilon}(E,i)$:

$$\sum_n A_n(E,i)H^0_{mn} + \sum_\alpha \int_{\varepsilon_c} B_{\alpha\varepsilon}(E,i)V_{m,\alpha\varepsilon}\,d\varepsilon = EA_m(E,i),$$

(5a)

$$\sum_n A_n(E,i)V_{\alpha\varepsilon,n} + \varepsilon B_{\alpha\varepsilon}(E,i) = EB_{\alpha\varepsilon}(E,i).$$

(5b)

This set of equations can be solved directly by the elimination method [13,25,26]. The trick is to apply the principal value to Eq. (5b):

$$B_{\alpha\varepsilon}(E,i) = \mathcal{P}\frac{\sum_n A_n(E,i)V_{\alpha\varepsilon,n}}{E-\varepsilon} + Z_\alpha(E,i)\delta(E-\varepsilon)$$

(6)

where $\mathcal{P}$ indicates that the principal value should be taken when being inserted into the integral of Eq. (5a), and $Z_\alpha(E,i)$ is a prefactor to be determined by matching the boundary condition. To simplify the discussion, compact matrix expressions are introduced and denoted by bold font, e.g., $\boldsymbol{A}(E,i) \equiv (\ldots, A_n(E,i), ..)^T$, $\boldsymbol{B}(E,i) \equiv (\ldots, B_{\alpha\varepsilon}(E,i), \ldots)^T$, $\boldsymbol{Z}(E,i) \equiv (\ldots, Z_\alpha(E,i), \ldots)^T$, and $\boldsymbol{V}(\varepsilon) \equiv (\ldots, V_{\alpha\varepsilon,n}, \ldots)$. In the matrix notations, Eq. (6) reads $\boldsymbol{B}(E,i) = \mathcal{P}\frac{\boldsymbol{V}(\varepsilon)\boldsymbol{A}(E,i)}{E-\varepsilon} + \boldsymbol{Z}(E,i)\delta(E-\varepsilon)$. Inserting Eq. (6) into Eq. (5a), we get a closed expression [with only free prefactors $\boldsymbol{Z}(E,i)$] for $\boldsymbol{A}(E,i)$:

$$\boldsymbol{A}(E,i) = (\boldsymbol{H}^0 + \boldsymbol{F}(E) - E\boldsymbol{1})^{-1}[-\boldsymbol{V}^T(E)\boldsymbol{Z}(E,i)]$$

(7)

where $\boldsymbol{1}$ is the unit matrix, and $\boldsymbol{F}(E) = \mathcal{P}\int_{\varepsilon_c} d\varepsilon\frac{\boldsymbol{V}^T(\varepsilon)\boldsymbol{V}(\varepsilon)}{E-\varepsilon}$ is called the residual term, with the integral region being the same as in Eqs. (4) and (5). The first two terms in the denominator together can simply be considered as an effective Hamiltonian $\boldsymbol{H}^b = \boldsymbol{H}^0 + \boldsymbol{F}$ for the non-Rydberg states after projecting out the continuum configurations [22,23,69]. The matrix elements are

$$H^b_{mn} = H^0_{mn} + F_{mn},$$

(8)

$$F_{mn} = \mathcal{P}\sum_\alpha \int_\varepsilon d\varepsilon\frac{V_{m,\alpha\varepsilon}V_{\alpha\varepsilon,n}}{E-\varepsilon}.$$

(9)

Diagonalizing the effective Hamiltonian $\boldsymbol{H}^b$ leads to a new shifted basis function for the non-Rydberg resonant states:

$$\boldsymbol{H}^b = \boldsymbol{G}^T\boldsymbol{e}\boldsymbol{G},$$

(10)

where $\boldsymbol{G}^T\boldsymbol{G} = \boldsymbol{1}$, and $\boldsymbol{e}$ the diagonal matrix with its elements the eigenvalues of $\boldsymbol{H}^b$. In this new basis, the coefficient solutions can be reformatted into a nicer form:

$$\boldsymbol{A}(E,i) = \boldsymbol{G}(E\boldsymbol{1}-\boldsymbol{e})^{-1}\tilde{\boldsymbol{v}}^T(E)\boldsymbol{Z}(E,i),$$

(11a)

$$\boldsymbol{B}(E,i) = \mathcal{P}\frac{\boldsymbol{\kappa}(\varepsilon,E)\boldsymbol{Z}(E,i)}{\pi(E-\varepsilon)} + \boldsymbol{Z}(E,i)\delta(E-\varepsilon)$$

(11b)

where $\tilde{\boldsymbol{v}}$ and $\boldsymbol{\kappa}(E,\varepsilon)$ abbreviate the following expression:

$$\tilde{\boldsymbol{v}} \equiv \boldsymbol{V}\boldsymbol{G} = \sum_k V_{\alpha,k}(E)G_{k,m},$$

(12a)

$$\boldsymbol{\kappa}(\varepsilon,E) \equiv \pi\tilde{\boldsymbol{v}}(\varepsilon)(E\boldsymbol{1}-\boldsymbol{e})^{-1}\tilde{\boldsymbol{v}}(E)^T$$

$$= \pi\sum_m\frac{\sum_n V_{\alpha\varepsilon,n}G_{n,m}\cdot\sum_k G_{k,m}V_{k,\beta E}}{E-e_m},$$

(12b)

and e_m is the element of $\boldsymbol{e}$.

The physical state wave function for the complete system including the non-Rydberg states can be obtained by directly inserting Eqs. (11) and (2) into Eq. (4). The reaction matrix $\boldsymbol{K}$ is directly related to the behavior of wave functions in the asymptotic limit (i.e., $r \to \infty$), where the constituent function Ψ^0_n for the bound states in the first summation vanishes, and the regular and irregular Coulomb functions f and g approximate $\sqrt{2/\pi k}\sin(kr+\theta)$ and $-\sqrt{2/\pi k}\cos(kr+\theta)$ respectively (θ being the Coulomb phase shift) [50,70]. The first part of the $\boldsymbol{B}$ coefficient is related to the so-called Hilbert transform, i.e., $H[f(E)] = \frac{1}{\pi}\mathcal{P}\int\frac{f(E)d\varepsilon}{E-\varepsilon}$, of the the asymptotic expression of Coulomb wave-function pairs [71], $\frac{1}{\pi}\mathcal{P}\int_{\varepsilon_c}\frac{f(r,\varepsilon)}{E-\varepsilon}d\varepsilon = g(r,E)$ as well as $\frac{1}{\pi}\mathcal{P}\int_{\varepsilon_c}\frac{g(r,\varepsilon)}{E-\varepsilon}d\varepsilon = -f(r,E)$(for $r \to \infty$). With these ingredients, the asymptotic wave function of the physical state now reads

$$\Psi(E,i) \xrightarrow{r\to\infty} \boldsymbol{Z}^T(E)\{\boldsymbol{\kappa}^T(E,E)(\boldsymbol{g}\boldsymbol{U}^0\cos\pi\boldsymbol{\mu}^0$$
$$+ \boldsymbol{f}\boldsymbol{U}^0\sin\pi\boldsymbol{\mu}^0)^T$$
$$+ (\boldsymbol{f}\boldsymbol{U}^0\cos\pi\boldsymbol{\mu}^0 - \boldsymbol{g}\boldsymbol{U}^0\sin\pi\boldsymbol{\mu}^0)^T\}\boldsymbol{\Theta}$$

(13a)

$$= \boldsymbol{Z}^T(E)\{\boldsymbol{f}[\boldsymbol{U}^0\sin\pi\boldsymbol{\mu}^0\boldsymbol{\kappa}(E,E) + \boldsymbol{U}^0\cos\pi\boldsymbol{\mu}^0]$$
$$- \boldsymbol{g}[\boldsymbol{U}^0\sin\pi\boldsymbol{\mu}^0 - \boldsymbol{U}^0\cos\pi\boldsymbol{\mu}^0\boldsymbol{\kappa}(E,E)]\}^T\boldsymbol{\Theta}$$

(13b)

$$\equiv [(\boldsymbol{f}\boldsymbol{X} - \boldsymbol{g}\boldsymbol{Y})\boldsymbol{Z}(E)]^T\boldsymbol{\Theta},$$

(13c)

where Eq. (13b) is simply the regrouping of the expression into $\boldsymbol{f}$ and $\boldsymbol{g}$ terms, respectively. By comparison with the definition of the reaction matrix [44,49,50,55], i.e., $\Psi(E,i) \propto \sum_{i'}\Theta_i f_i(r)\delta_{ii'} - \Theta_{i'}g'_i(r)K_{ii'}(r > r_0)$, the perturbed $\boldsymbol{K}$ matrix is easily obtained by taking out the prefactor matrix $\boldsymbol{X}$ associated with the $\boldsymbol{f}$ terms in Eq. (13):

$$\Psi(E,i) \xrightarrow{r\to\infty} [(\boldsymbol{f} - \boldsymbol{g}\boldsymbol{Y}\boldsymbol{X}^{-1})\boldsymbol{X}\boldsymbol{Z}(E)]^T\boldsymbol{\Theta},$$

(14)

$$\boldsymbol{K} = \boldsymbol{Y}\boldsymbol{X}^{-1}$$
$$= [\boldsymbol{U}^0\sin\pi\boldsymbol{\mu}^0 - \boldsymbol{U}^0\cos\pi\boldsymbol{\mu}^0\boldsymbol{\kappa}(E,E)]$$
$$\times [\boldsymbol{U}^0\cos\pi\boldsymbol{\mu}^0 + \boldsymbol{U}^0\sin\pi\boldsymbol{\mu}^0\boldsymbol{\kappa}(E,E)]^{-1}.$$

(15)

Finally, the scattering matrix parameters $\{U_{i\alpha}, \mu_\alpha\}$ of the full system, which changes rapidly with energy (indicating the presence of resonances), can be obtained by diagonalizing the $\boldsymbol{K}$ matrices. These $\boldsymbol{K}$ matrices are easily constructed from smooth functions of energy, $\Phi^0_{\alpha\varepsilon}$, $U^0_{i\alpha}$, $\pi\mu^0_\alpha$, and $V_{\alpha\varepsilon,n}$ using basic algebraic operations. Therefore, rich physical quantities, such as the energy levels as well as cross sections of photoabsorption, collisional excitation, dielectronic recombination, etc., can then be accurately calculated by solving the MQDT equations [44,49,50,55,57].

The effectiveness and correctness of the nonperturbative approach are demonstrated by comparing the calculated scattering matrix parameters with those obtained from full R-R-eigen calculations for the $e + \text{O}^+$ system with symmetry block $J^\pi = 1^-$ as an example in Fig. 2. In the energy
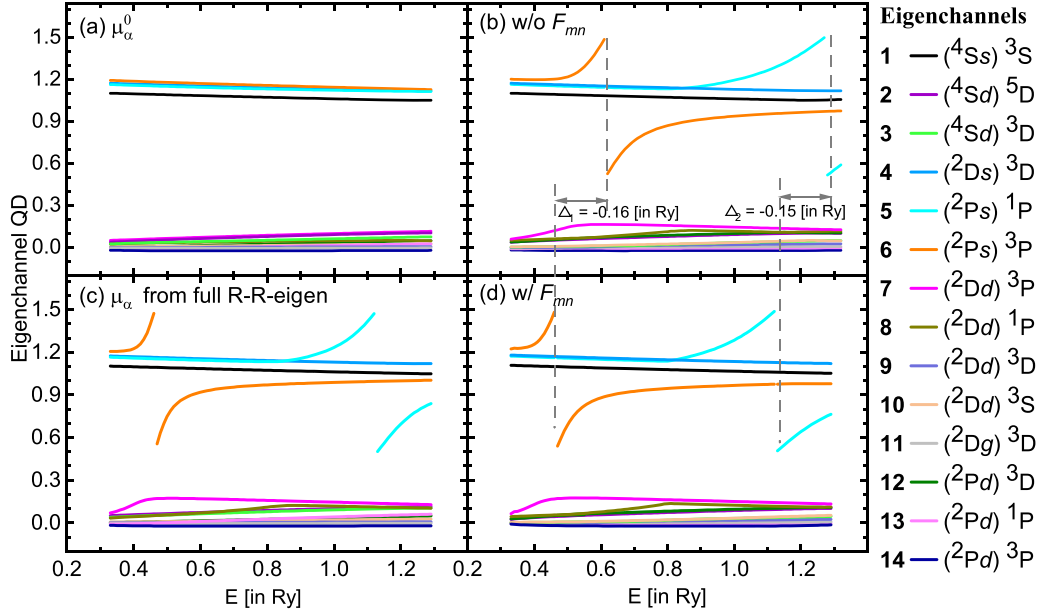
FIG. 2. Quantum defects for an atomic oxygen system with non-Rydberg resonances in different treatments. (a) Pure-continuum type eigenchannel quantum defects (EQDs) μ_α^0 obtained from R-R-eigen calculation. (b) EQD obtained with our approach but taking the residual interaction term F_{mn} out of Eq. (7) to demonstrate its effect. (c) EQD obtained from full R-R-eigen calculations. (d) EQD obtained in the approach with the F_{mn} term. The shifts ($\Delta_1 = -0.16$ and $\Delta_2 = -0.15$ Ry for $2s2p_{1/2}^2 2p_{3/2}^3$ and $2s2p_{1/2}^1 2p_{3/2}^4$, respectively) of the resonant structures due to the terms F_{mn} are indicated by the dashed lines.

range of interest, 14 ionization channels (JJ notation) and the corresponding eigenchannels (LS notation) are relevant. Their detailed designation can be found in Table I. The pure-continuum eigenchannel quantum defects (EQDs) μ_α^0 shown in Fig. 2(a) vary smoothly with energy, whereas two resonances appear in (c) for the EQD μ_α obtained from the full R-R-eigen calculations with two non-Rydberg states $2s2p_{1/2}^2 2p_{3/2}^3$ at around 0.45 Ry and $2s2p_{1/2}2p_{3/2}^4$ at around 1.1 Ry respectively. The EQD obtained from the nonperturbative approach shown in (d) reproduces the R-R-eigen calculations very well with less computational effort. To demonstrate the effect of the residual interaction F_{mn} induced by the coupling of the non-Rydberg states with eigenchannels, the term F_{mn} in the denominator in Eq. (8) is removed. As a result, the two resonances in the calculated EQD shown in (b) are blueshifted with respect to the true EQD calculated by following the original recipe. Note that since the residual interaction F_{mn} shows near-constant dependence of energy, it can be approximated as a constant in the practical calculation, which can further improve the computational efficiency. This

verifies the effectiveness of treating the non-Rydberg resonant states in our analytical nonperturbative approach.

C. Multichannel quantum defect theory

To demonstrate the calculation for the physical states after obtaining the MQDT parameters, we start with the eigenchannel wave function $\Psi_\alpha^{J\pi}$, which can be calculated variationally within the reaction zone ($r \leqslant r_0$). Outside the reaction zone ($r \geqslant r_0$) it can be rigorously expressed as [44–48,50]

$$\Psi_\alpha^{J\pi} = \sum_{i=1}^N \Phi_i U_{i\alpha}(f_i \cos \pi \mu_\alpha - g_i \sin \pi \mu_\alpha), \quad r \geqslant r_0 \quad (16)$$

where f_i and g_i are the regular and irregular Coulomb functions, respectively, and Φ_i is the channel wave function. The energy eigen wavefunction $\Psi^{J\pi}(E)$ can be described as a linear combination of the eigenchannel wave functions:

$$\Psi^{J\pi}(E) = \sum_\alpha A_\alpha(E)\Psi_\alpha^{J\pi}(E), \quad (17)$$

TABLE I. The physical channels (ionization channel) and corresponding eigenchannels for O with $J^\pi = 1^-$.

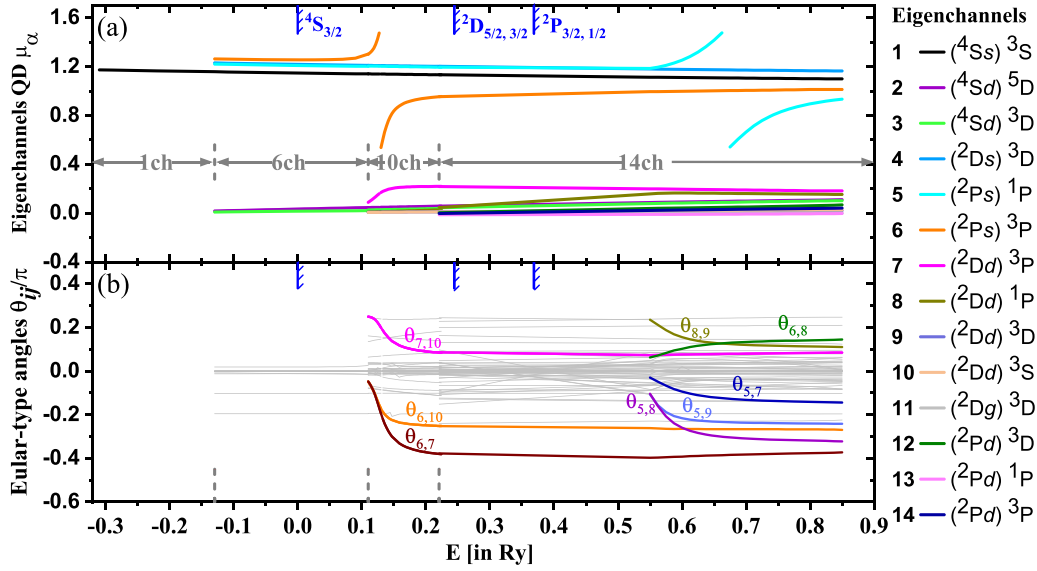| Parameter	Value						
Index	1	2	3	4	5	6	7
Ionization channels	$^4S_{3/2}s_{1/2}$	$^4S_{3/2}d_{3/2}$	$^4S_{3/2}d_{5/2}$	$^2D_{3/2}s_{1/2}$	$^2P_{3/2}s_{1/2}$	$^2P_{1/2}s_{1/2}$	$^2D_{5/2}d_{3/2}$
Eigenchannels	$^4Ss\ ^3S$	$^4Sd\ ^5D$	$^4Sd\ ^3D$	$^2Ds\ ^3D$	$^2Ps\ ^1P$	$^2Ps\ ^3P$	$^2Dd\ ^3P$
Index	8	9	10	11	12	13	14
Ionization channels	$^2D_{5/2}d_{5/2}$	$^2D_{3/2}d_{3/2}$	$^2D_{3/2}d_{5/2}$	$^2D_{5/2}g_{7/2}$	$^2P_{3/2}d_{3/2}$	$^2P_{3/2}d_{5/2}$	$^2P_{1/2}d_{3/2}$
Eigenchannels	$^2Dd\ ^1P$	$^2Dd\ ^3D$	$^2Dd\ ^3S$	$^2Dg\ ^3D$	$^2Pd\ ^3D$	$^2Pd\ ^1P$	$^2Pd\ ^3P$

FIG. 3. MQDT parameters (scattering matrices) for the $e + O^+$ system with $J^\pi = 1^-$ in both discrete and autoionization energy regions $[-0.31 \leqslant E$ (in Ry) $< 0.85]$ across five thresholds (blue shaded lines). (a) Eigenchannel quantum defects μ_α. (b) Euler-type angles θ_{ij} representing the transformation matrix $U_{i\alpha}$. The highlighted curves demonstrate the strong interchannel interactions. The calculation is divided into four energy regions, each region labeled with the number of physical channels, i.e., 1ch, 6ch, 10ch, and 14ch.

where A_α is the mixing coefficient to be determined by asymptotic boundary conditions [44–48,50] in the MQDT method. The nontrivial solution of the MQDT equations leads to a determinant equation:

$$F(\{\nu_i\}, \{\mu_\alpha, U_{i,\alpha}\}) = \det[U_{i\alpha} \sin \pi(\nu_i + \mu_\alpha)] = 0 \quad (18)$$

with the effective principal quantum numbers ν_i defined by the energy relations

$$E = I_i - \frac{q^2}{\nu_i^2}, \quad (19)$$

where I_i is the corresponding threshold (in Ry) and q is the charge of the target.

Then, all discrete energy levels and autoionization resonances in the entire channel can be systematically obtained using the semianalytical JHANGZ [namely projected high-dimensional quantum-defect graph (symmetrized)] plot method [57] for solving MQDT equations with multithreshold. This graphical method facilitates the direct comparison of theoretical energy levels and resonances with available precision spectroscopic measurement data [64]. On the other hand, we can easily determine the precision of scattering calculations systematically based on the analytical continuation property of the short-range scattering matrix.

III. APPLICATION TO THE OXYGEN SYSTEM

A. Short-range scattering matrix parameters

Our nonperturbative approach is applied to study both spectroscopy and the scattering phenomena in the oxygen system with symmetry block $J^\pi = 1^-$, where two non-Rydberg states are present. Moreover, we reveal the relationship between the numerical accuracy of the eigenchannels and the non-Rydberg states by designing a series of calculation models of successively increasing complexity and measuring the

numerical accuracy of each channel accordingly. Specifically, ten calculation models are constructed by considering different degrees of electronic correlations in the target states and by including different numbers of target states. The target states are optimized layer by layer using our developed quasicomplete basis sets (QCBS) scheme [72–74]; the details can be found in the Appendix. In the energy range of interest, 14 eigenchannels listed in Table I are relevant; as will be shown in the next subsection, the calculated short-range scattering matrix parameters in model 6 are found to agree the best with spectroscopic observations. The corresponding EQD μ_α and Euler-type angles θ_{ij}, representing the transformation matrix $U_{i\alpha}$, are shown in Figs. 3(a) and 3(b), respectively. It can be seen that the scattering parameters vary smoothly over the energy range across the five target ionization thresholds, indicated by the blue shade lines. Due to the analytical property of the short-range scattering matrix, the scattering matrix parameters smoothly interface into higher-energy regions with a larger number of physical channels [51–53,55,56]. The resonances appear mainly in the 10ch and 14ch energy regions for the eigenchannels (^2Ps) ^3P and (^2Ps) ^1P, due to perturbations by non-Rydberg resonant states $2s2p^5$ ^3P and ^1P, respectively.

B. MQDT analysis of spectroscopic phenomena

To obtain the physical states directly, and to gauge the numerical accuracy against the precise experimental spectroscopic levels, we use the MQDT procedure to project the high-dimensional scattering matrix parameters onto two-dimensional plots with the JHANGZ graphical method [75]. The JHANGZ plot for the energy regions with one, six, and ten channels $[-0.31 \leqslant E$ (in Ry) < 0.220, corresponding to $1.3 \leqslant \nu_{2D_{5/2}} < 6.4]$ is presented in Fig. 4. We chose an appropriate two-dimensional plot with $\nu_{2D_{5/2}}$ versus $-\nu_{4S_{3/2}}$, because we focus on the two strongly perturbed Rydberg series, $^4S_{3/2}$ nd and $^2D_{5/2}$ nd. As a result, the energy relation
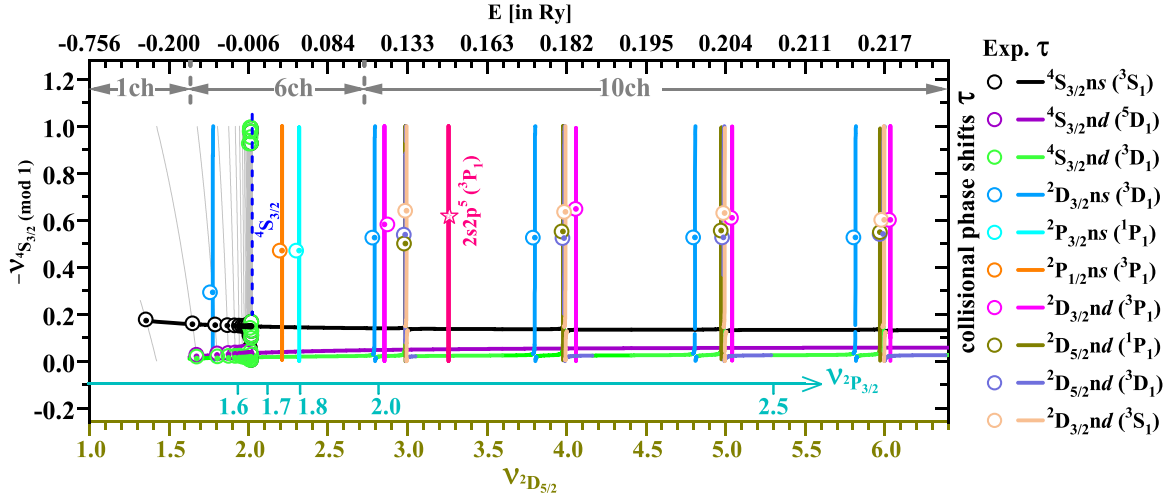
FIG. 4. MQDT analysis for the $e + O^+$ system in the energy range of $-0.31 \leqslant E$ (in Ry) < 0.220 (i.e. $1.3 \leqslant \nu_{2D_{5/2}} < 6.4$). Three horizontal lines with quasiperiodic resonant structures are the effective eigenphase shifts obtained from the MQDT Eq. (18). Gray line segments denote the energy relation Eq. (19) between $\nu_{2D_{5/2}}$ and $-\nu_{4S_{3/2}}$. Theoretical energy levels and autoionization resonances denoted by the small dots show excellent agreement with spectroscopic observations marked as larger hollow symbols. The red star denotes the non-Rydberg resonance state $2s2p^5 \; ^3P$.

between the thresholds $^4S_{3/2}$ and $^2D_{5/2}$. i.e., $I_{2D_{5/2}} - q^2/\nu^2_{2D_{5/2}} = I_{4S_{3/2}} - q^2/\nu^2_{4S_{3/2}}$ from Eq. (19), is shown as a series of gray line segments converging to $^4S_{3/2}$, represented as a brown dashed line. Auxiliary abscissas associated with the fourth threshold $\nu_{2P_{3/2}}$ are also plotted to help characterize the corresponding Rydberg series associated with the ^2P target states. Three horizontal lines with quasiperiodic steep resonance structures are the solution of the MQDT Eq. (18). The black, red, and green curves represent three effective eigenchannels (collisional eigenchannels [45,48]) associated with the first ionization threshold, i.e., $^4Ss \; (^3S_1)$, $^4Sd \; (^5D_1)$, and $^4Sd \; (^3D_1)$, respectively. The color of the resonances encodes their major eigenchannel contribution based on the wave-function analysis of A_α in Eq. (17). The cross points between the gray energy relation curves and the colored eigenphase shifts marked by small full dots are the theoretical energy levels. As for the autoionization resonances, their energy positions (ν^r, τ^r_ρ) are defined as the maxima of the energy derivatives of the eigenphase shift [58], i.e., $\pi \frac{d\tau_\rho}{dE}|_{max} = \pi (\nu^3 \frac{d\tau_\rho}{d\nu})|_{\nu^r}$. The available precise experimental spectroscopic observations [64] are denoted by larger hollow symbols for benchmark comparison. Among them, the non-Rydberg resonant state $2s2p^5 \; ^3P$ is denoted as a pink star. As is shown clearly, all bound states as well as autoionizations, including the non-Rydberg resonance, show excellent agreement with the experimental data. All autoionization states in the 14-channel energy regions are also obtained, but for brevity their JHANGZ analysis is omitted here and they are used only to evaluate the accuracies of the scattering matrices in the next subsection.

C. Influences of the non-Rydberg resonant states on the coupled eigenchannels

With the nonperturbative approach as an extension of MQDT, we can study the influence of the non-Rydberg states on the overall calculation accuracy. We define the scattering

matrix inaccuracy as the absolute value of the shift of the EQD that minimizes the overall discrepancy between the theoretical and experimental energy levels as well as the autoionization resonances [64]:

$$S_{acc} = \left| \mu_\alpha^{exp} - \mu_\alpha^{theo} \right|. \qquad (20)$$

The acceptance value of the optimization procedure is set to the experimental measurement uncertainty, approximately $\pm 2 \; cm^{-1}$ [76].

The evaluated inaccuracies of the scattering matrices, S_{acc}, for eigenchannels strongly perturbed and unperturbed by the non-Rydberg states are shown separately in Fig. 5 to illustrate the influence of the non-Rydberg states on the overall numerical accuracy of the neutral oxygen system with $J^\pi = 1^-$. Ten calculation models with increasing complexity indicated by the model index are included in the paper. It can be seen that S_{acc} does not decrease monotonously with the increasing model complexity. In addition, the result shown in subfigures (b) and (c) lying energetically closer to the two non-Rydberg resonant states shows much bigger inaccuracies than the inaccuracy for the same channels in the 6ch region. However, the unperturbed channels behave more or less identically for all three energy regions. Therefore, we show only the 14ch as an example. These behaviors suggest that the non-Rydberg resonant states have a significant influence on the numerical accuracy of the perturbed channels.

To further investigate the influence of non-Rydberg states on the overall computational inaccuracy, we need to introduce an intuitive evaluation scheme for the numerical inaccuracy of both the non-Rydberg states and the eigenchannel states. The overall numerical inaccuracy S_{acc}^{tot} for the eigenchannel states is simply defined by averaging over the channels with the number of experimentally observed spectroscopy states in each channel as the statistical weights. The overall numerical inaccuracy S_{acc}^{tot} is evaluated for each of the ten calculation models and is shown in Fig. 6(a). The numerical inaccuracy for the non-Rydberg states is defined by the deviation of the
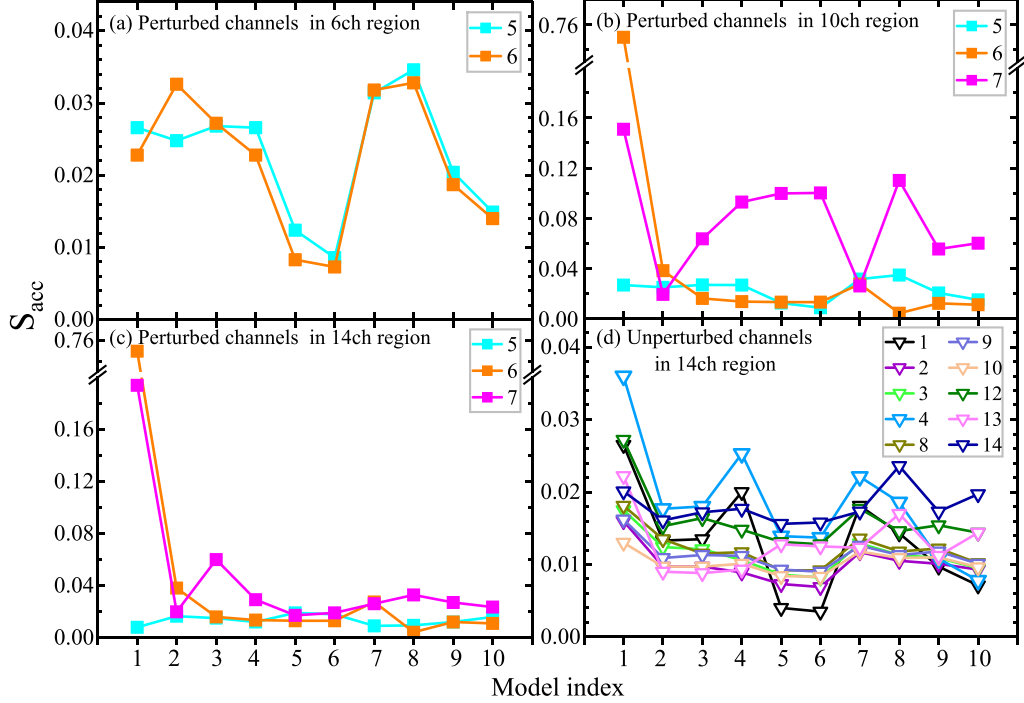
FIG. 5. The inaccuracies of the scattering matrices S_{acc} for the ten calculation models. The calculation inaccuracy is found strongly related to the coupling strength with the non-Rydberg resonant states. (a)–(c) The eigenchannels strongly perturbed by non-Rydberg states in the 6ch, 10ch, and 14ch regions. (d) Unperturbed channels in the 14ch region.

theoretical energy position of the non-Rydberg states E_{theo} from the experimental values E_{exp} [64,77]. The inaccuracy is further averaged over the singlet ^1P and triplet ^3P states:

$$Q_{non} = \tfrac{1}{2}\left(\left|E_{theo}^{3P} - E_{exp}^{3P}\right| + \left|E_{theo}^{1P} - E_{exp}^{1P}\right|\right). \tag{21}$$

The evaluated inaccuracies for the ten calculation models are shown in Fig. 6(b). The inaccuracy of both Rydberg and non-Rydberg states does not show a monotonically decreasing trend with increasing model complexity, as indicated by the model indices. Instead, the most reliable results are obtained with model 6, where the optimal balance between the precision of the non-Rydberg resonant states and the overall accuracy of the normal Rydberg-type states is obtained. In summary, this demonstrates the importance of the treatment of non-Rydberg states within atomic systems, which not only affect the quality of their energy positions but also propagate their inaccuracies to other normal Rydberg states due to strong electronic correlations.

IV. CONCLUSION

In this paper, we proposed an efficient nonperturbative approach to treat the non-Rydberg states in the framework of MQDT, which can be considered as an extension of the MQDT method. Our approach consists of two steps. First, we calculate the scattering matrices excluding the bound-type configurations by the relativistic eigenchannel R-matrix method (R-R-eigen) on sparse energy grids. The scattering matrices are smooth functions of the energy. Second, the scattering matrix for the whole system is obtained by restoring the configuration interactions of the previously omitted bound-type configurations with the calculated pure-continuum-type eigenchannels in Eq. (14), which is similar to Fano's configuration-interaction procedure [13,22–26]. For details of the theoretical derivation, see Sec. II. In the present approach, only low-dimensional matrix operations are involved without repeatedly calculating the R matrix for dense energies. This feature makes our approach highly efficient and flexible for the calculation of the structure and scattering
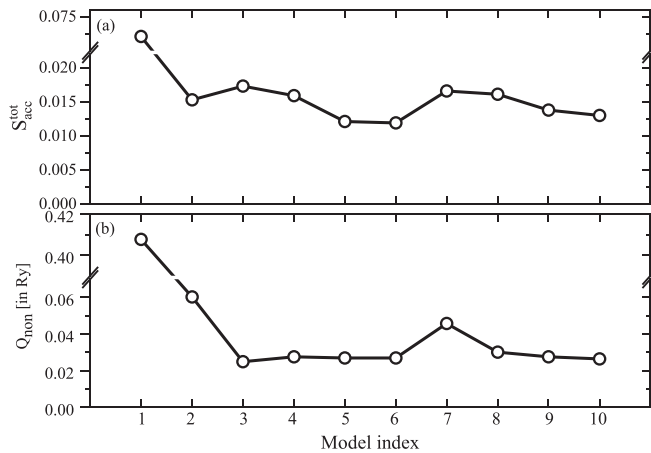

FIG. 6. Calculation inaccuracy for (a) overall inaccuracies of the scattering matrices S_{acc}^{tot}, evaluated by a weighted-averaging algorithm for all the channels, and (b) the averaged energy position of the two non-Rydberg resonant states $2s2p^5\ ^3P_1$ and $^1P_1$.

TABLE II. Six levels of QCBSs for the ionic target states and corresponding ten *R-R*-eigen calculation models defined by the number of target states.

Parameter	Basis set index									
	I	II	III	IV		V		VI		
Configurations[a]	$2s^22p^3$	$2s^22p^3$	$2s^22p^3$	$[2s^22p^3 - \widetilde{3s}\widetilde{3p}]$S, D		$[2s^22p^3 - \widetilde{3l}]$S, D		$[2s^22p^3 - \widetilde{3l}\widetilde{4l}]$S, D		
		$[2s^12p^4]$S, D	$[2s^12p^4]$S, D	$[2s^12p^4 - \widetilde{3s}\widetilde{3p}]$S, D		$[2s^12p^4 - \widetilde{3l}]$S, D		$[2s^12p^4 - \widetilde{3l}\widetilde{4l}]$S, D		
			$[2p^5]$S, D	$[2s^22p^33s - \widetilde{3s}\widetilde{3p}]$S, D		$[2s^22p^33s - \widetilde{3l}]$S, D		$[2s^22p^33s - \widetilde{3l}\widetilde{4l}]$S, D		
Number of targets[b]	5	13	15	15	46	57	15	46	15	46
Index of models	1	2	3	4	5	6	7	8	9	10

[a]Configuration space for each QCBS: nl, principal and angular quantum numbers for spectroscopic orbitals; $\widetilde{nl}$, principal and angular quantum numbers for the extended pseudo-orbitals; S, single-electron excitation; D, double-electron excitation.
[b]The total number of physical and computational targets considered in the *R-R*-eigen calculation, where the first five target states $\{^4S_{3/2}, {}^2D_{5/2,3/2}, {}^2P_{3/2,1/2}\}$ of the ground-state configuration $2s^22p^3$ for O^+ are the physical targets.

processes including non-Rydberg resonant states. In addition, our approach allows us to check and calibrate all bound states and autoionization resonances, including the non-Rydberg ones, against the spectroscopic measurements in a unified manner using the semianalytical graphical MQDT procedures, namely the JHANGZ plot [57].

Our method is applied to the calculation of the challenging electron collision with singly charged oxygen ion (e + O^+) problem for the symmetry block $J^\pi = 1^-$, where two non-Rydberg states ($^3P_1^o$ and $^1P_1^o$) are present for the $2s^12p^5$ configuration. With the bound-continuum interaction matrices and pure-continuum eigenchannel MQDT parameters, the eigenchannel scattering matrix including the non-Rydberg resonances is obtained and shown in Fig. 3. By applying the graphical solution of the MQDT equations of the scattering matrices, the bound and autoionization states are all obtained in Fig. 4, which shows excellent agreement with existing spectroscopic measurements.

With this efficient method, we can further analyze the influence of the non-Rydberg resonances on the accuracy of the calculations in Sec. III C. We show that the non-Rydberg states are the main reason for the puzzling accuracy dilemma in the atomic oxygen system, where the higher computational effort would not promise better agreement with experimental observations. Figure 5 shows that the channels strongly coupled to the non-Rydberg states are more prone to be plagued by the less accurate non-Rydberg states. The propagation of inaccuracy manifests itself in such a way that simply increasing the computational targets for these channels would not improve their accuracy. Instead, it is found that the best agreement with the experiment is achieved by a medium-scale calculation that optimally balances the precision of the non-Rydberg resonant states with that of the Rydberg states.

In summary, we have developed a nonperturbative approach for the efficient calculation of the non-Rydberg states in the MQDT framework. In combination with the proposed estimation of calculation inaccuracy, we can calibrate and improve the calculation with the presence of non-Rydberg states against the existing experimental spectroscopic measurements. This method will provide highly accurate atomic oxygen oscillator strength data, including the non-Rydberg

states, to solve the problem of diagnosing the electron density in astro-objects.

APPENDIX

In the present paper, the atomic orbitals (AOs) for the target states are calculated using the quasicomplete basis scheme (QCBS) extended layer by layer using multiconfiguration self-consistent field (MCSCF) methods [2,72–74,78], using our extended GRASP-JT program based on GRASP-2K code [79]. Details of the calculation schemes for the QCBS of the target (O^+ ion) are listed in Table II. In QCBS I, all AOs of the ground-state configuration $2s^22p^3$ are obtained as spectroscopic orbitals. For QCBS II and III, we choose $\{2s^22p^3, 2s^12p^4\}$ and $\{2s^22p^3, 2s^12p^4, 2p^5\}$ as reference configurations to extend the configuration state functions and to optimize all levels by the extended optimal level in the MCSCF calculation, respectively.

To account for adequate electronic correlations, more and more AOs are included in QCBS IV, V, and VI, in addition to the fixed wave functions for spectroscopic orbitals $\{1s, 2s, 2p\}$ optimized in QCBS I. In QCBS IV, the AOs sets are extended to $\widetilde{3s}$ and $\widetilde{3p}$ (here tilde orbitals mean that they are pseudo-orbitals) by single (S) and double (D) substitution of electrons from orbitals in reference configuration $\{2s^22p^3, 2s^12p^4, 2s^22p^23s\}$ to the specific active orbital set $\{\widetilde{3s}\widetilde{3p}\}$. Similarly, $\widetilde{3d}$ and $\widetilde{4l}$ are included in QCBS V and VI respectively. In the optimization of each QCBS stage, we optimize only the newly added orbitals and keep the previously decided orbitals fixed.

The theoretical energies for the first five states obtained from the six QCBSs are listed in Table III. The relative energies to the ground states compared to the experimental values from NIST [64] are also listed in the table. It can be seen that the calculated results converge to the experimental data (within 3% for QCBS VI) as the active space increases.

In our *R-R*-eigen calculation, the number of computational targets determines the number of computational

TABLE III. Total energies for the five physical target states in six different QCBSs and their relative differences to the ground states in comparison with experimental values.

Parameter	Excitation	Basis set index					
		I	II	III	IV	V	VI
Total energy (Ry)	$^4S_{3/2}$	−148.8546	−148.8513	−148.8514	−148.9296	−149.0568	−149.0998
	$^2D_{5/2}$	−148.5790	−148.5783	−148.5783	−148.6559	−148.7930	−148.8485
	$^2D_{3/2}$	−148.5790	−148.5783	−148.5783	−148.6560	−148.7931	−148.8486
	$^2P_{3/2}$	−148.3952	−148.3962	−148.4813	−148.5670	−148.6694	−148.7234
	$^2P_{1/2}$	−148.3953	−148.3963	−148.4813	−148.5670	−148.6694	−148.7234
Relative difference (%)[a]	$^4S_{3/2}$						
	$^2D_{5/2}$	12.71	11.75	11.79	12.00	7.97	2.84
	$^2D_{3/2}$	12.81	11.65	11.69	11.89	7.86	2.74
	$^2P_{3/2}$	24.55	23.40	0.35	−1.67	5.06	2.06
	$^2P_{1/2}$	24.57	23.37	0.34	−1.67	5.05	2.05

[a]The relative deviations between the theoretical values and the experimental values from NIST [64].

channels used to consider adequate electronic correlations. All five target states {$^4S_{3/2}$, $^2D_{5/2,3/2}$, $^2P_{3/2,1/2}$} of the O$^+$ ground-state configuration $2s^2 2p^3$ are used as physical target states, forming 14 physical channels with the excited electron in a specific energy region with total angular momentum $J^\pi = 1^-$. The details of the computational targets are listed in the fifth row of Table II; for QCBS I, II, and III all available states are taken as target states, meaning that they have 5, 13, and 15 computational targets, respectively. For QCBS IV, V, and VI, we experiment with a different limited number of states to be taken as target states.

[1] M. J. Seaton and D. E. Osterbrock, Astrophys. J. **125**, 66 (1957).

[2] X. Y. Han, X. Gao, D. L. Zeng, J. Yan, and J. M. Li, Phys. Rev. A **85**, 062506 (2012).

[3] S. S. Tayal, Astrophys. J., Suppl. Ser. **171**, 331 (2007).

[4] M. Montenegro, W. Eissner, S. N. Nahar, and A. K. Pradhan, J. Phys. B **39**, 1863 (2006).

[5] R. Kisielius, P. J. Storey, G. J. Ferland, and F. P. Keenan, Mon. Not. R. Astron. Soc. **397**, 903 (2009).

[6] G. Wallerstein, I. Iben, P. Parker, A. M. Boesgaard, G. M. Hale, A. E. Champagne, C. A. Barnes, F. Käppeler, V. V. Smith, R. D. Hoffman, F. X. Timmes, C. Sneden, R. N. Boyd, B. S. Meyer, and D. L. Lambert, Rev. Mod. Phys. **69**, 995 (1997).

[7] J. Lindl et al., Nucl. Fusion **51**, 094024 (2011).

[8] J. Lindl, O. Landen, J. Edwards, E. Moses, and N. Team, Phys. Plasmas **21**, 020501 (2014).

[9] J. F. Wu, W. Y. Miao, L. F. Wang, Y. T. Yuan, Z. R. Cao, W. H. Ye, Z. F. Fan, B. Deng, W. D. Zheng, M. Wang, W. B. Pei, S. P. Zhu, S. E. Jiang, S. Y. Liu, Y. K. Ding, W. Y. Zhang, and X. T. He, Phys. Plasmas **21**, 042707 (2014).

[10] H. Zhang, D. Yang, P. Song, S. Zou, Y. Zhao, S. Li, Z. Li, L. Guo, F. Wang, X. Peng, H. Wei, T. Xu, W. Zheng, P. Gu, W. Pei, S. Jiang, and Y. Ding, Phys. Plasmas **21**, 112709 (2014).

[11] R. Aymar, Plasma Phys. Control. Fusion **42**, B385 (2000).

[12] J. Bauche, C. Bauche-Arnoult, and O. Peyrusse, Atomic Properties in Hot Plasmas, 1st ed. (Springer, New York, 2015).

[13] U. Fano, Phys. Rev. **124**, 1866 (1961).

[14] P. Burke and W. Robb, The R-Matrix Theory of Atomic Processes (Academic, New York, 1976).

[15] A. V. Glushkov, O. Y. Khetselius, and A. A. Svinarenko, Phys. Scr. **T153**, 014029 (2013).

[16] U. Becker and D. A. Shirley, VUV and Soft X-Ray Photoionization (Springer, New York, 2012).

[17] J. Dubau and S. Volonte, Rep. Prog. Phys. **43**, 199 (1980).

[18] C. M. Lee, Phys. Rev. A **16**, 109 (1977).

[19] A. Giusti, J. Phys. B **13**, 3867 (1980).

[20] A. Florescu-Mitchell and J. Mitchell, Phys. Rep. **430**, 277 (2006).

[21] T. Fujimoto, Plasma Spectroscopy (Oxford University, New York, 2004).

[22] H. Feshbach, Ann. Phys. (NY) **5**, 357 (1958).

[23] H. Feshbach, Ann. Phys. (NY) **19**, 287 (1962).

[24] H. Feshbach, Ann. Phys. (NY) **43**, 410 (1967).

[25] F. H. Mies, Phys. Rev. **175**, 164 (1968).

[26] L. C. Davis and L. A. Feldkamp, Phys. Rev. B **15**, 2961 (1977).

[27] W. Domcke, Phys. Rep. **208**, 97 (1991).

[28] W. Eissner and M. J. Seaton, J. Phys. B **5**, 2187 (1972).

[29] M. J. Seaton, J. Phys. B **7**, 1817 (1974).

[30] M. Crees, M. Seaton, and P. Wilson, Comput. Phys. Commun. **15**, 23 (1978).

[31] I. Bray and A. Stelbovics, Adv. At. Mol. Opt. Phys. **35**, 209 (1995).

[32] D. V. Fursa and I. Bray, J. Phys. B **30**, 757 (1997).

[33] K. Bartschat, Comput. Phys. Commun. **114**, 168 (1998).

[34] O. Zatsarinny, Comput. Phys. Commun. **174**, 273 (2006).

[35] P. G. Burke, R-Matrix Theory of Atomic Collisions: Application to Atomic, Molecular and Optical Processes (Springer-Verlag, Heidelberg, 2011).

[36] U. Fano and F. Prats, Proc. Nat. Acad. Sci. (India) **A33**, 553 (1963).

[37] P. L. Altick and E. N. Moore, Phys. Rev. **147**, 59 (1966).

[38] A. F. Starace, Phys. Rev. A **2**, 118 (1970).

[39] Y. Komninos and C. A. Nicolaides, Phys. Rev. A **34**, 1995 (1986).

[40] R. Moccia and P. Spizzo, Phys. Rev. A **43**, 2199 (1991).

[41] T. K. Fang and T. N. Chang, Phys. Rev. A **61**, 062704 (2000).

[42] W. Huang, Y. Zou, X. M. Tong, and J. M. Li, Phys. Rev. A **52**, 2770 (1995).

[43] X. M. Tong, J. M. Li, and Y. Zou, Acta Phys. Sin. **44**, 50 (1995) (in Chinese).

[44] U. Fano, J. Opt. Soc. Am. **65**, 979 (1975).

[45] C. M. Lee and K. T. Lu, Phys. Rev. A **8**, 1241 (1973).

[46] U. Fano and C. M. Lee, Phys. Rev. Lett. **31**, 1573 (1973).

[47] C. M. Lee, Phys. Rev. A **10**, 584 (1974).

[48] C. M. Lee and W. R. Johnson, Phys. Rev. A **22**, 979 (1980).

[49] M. J. Seaton, Rep. Prog. Phys. **46**, 167 (1983).

[50] M. Aymar, C. H. Greene, and E. Luc Koenig, Rev. Mod. Phys. **68**, 1015 (1996).

[51] X. Gao and J. M. Li, Chin. Phys. Lett. **29**, 033101 (2012).

[52] X. Gao and J. M. Li, Phys. Rev. A **89**, 022710 (2014).

[53] X. Gao, R. Jin, D. L. Zeng, X. Y. Han, J. Yan, and J. M. Li, Phys. Rev. A **92**, 052712 (2015).

[54] T. N. Chang, T. K. Fang, and X. Gao, Phys. Rev. A **91**, 023403 (2015).

[55] X. Gao, X. Y. Han, and J. M. Li, J. Phys. B **49**, 214005 (2016).

[56] D. L. Zeng, R. Jin, C. Gu, X. F. Yue, X. Gao, and J. M. Li, Phys. Rev. A **95**, 042508 (2017).

[57] R. Jin, X. Y. Han, X. Gao, D. L. Zeng, and J. M. Li, Sci. Rep. **7**, 11589 (2017).

[58] L. J. Dou, R. Jin, R. Sun, L. Y. Xie, Z. K. Huang, J. M. Li, X. W. Ma, and X. Gao, Phys. Rev. A **101**, 032508 (2020).

[59] K. A. Berrington, P. G. Burke, K. Butler, M. J. Seaton, P. J. Storey, K. T. Taylor, and Y. Yan, J. Phys. B **20**, 6379 (1987).

[60] K. A. Berrington, W. B. Eissner, and P. H. Norrington, Comput. Phys. Commun. **92**, 290 (1995).

[61] J. J. Chang, J. Phys. B **10**, 3335 (1977).

[62] P. H. Norrington and I. P. Grant, J. Phys. B **20**, 4869 (1987).

[63] S. Ait-Tahar, I. P. Grant, and P. H. Norrington, Phys. Rev. A **54**, 3984 (1996).

[64] A. Kramida, Y. Ralchenko, J. Reader, and NIST ASD Team, NIST Atomic Spectra Database (Ver. 5.11), https://physics.nist.gov/asd [January 31, 2016], National Institute of Standards and Technology, Gaithersburg, MD (2023).

[65] F. H. Mies, Phys. Rev. A **20**, 1773 (1979).

[66] P. F. O'Mahony, Phys. Rev. A **32**, 908 (1985).

[67] Q. B. Lu, *New Theories and Predictions on the Ozone Hole and Climate Change* (World Scientific, Singapore, 2015).

[68] R. P. Wayne, Res. Chem. Intermed. **20**, 395 (1994).

[69] V. I. Kukulin, V. M. Krasnopol'sky, and J. Horáček, *Theory of Resonances* (Springer, New York, 1989).

[70] K. T. Lu, Phys. Rev. A **4**, 579 (1971).

[71] V. A. Ditkin and A. P. Prudnikov, *Integral Transforms and Operational Calculus*, edited by I. N. Sneddon (Pergamon, New York, 1965).

[72] B. Qing, C. Cheng, X. Gao, X. L. Zhang, and J. M. Li, Acta Phys. Sin. **59**, 4547 (2010) (in Chinese).

[73] C. Cheng, X. L. Zhang, X. Gao, B. Qing, and J. M. Li, J. Phys. B **43**, 105001 (2010).

[74] C. Cheng, X. Gao, B. Qing, X. L. Zhang, and J. M. Li, Chin. Phys. B **20**, 033103 (2011).

[75] A. Magunia *et al.*, Sci. Adv. **9**, eadk1482 (2023).

[76] R. E. Huffman, J. C. Larrabee, and Y. Tanaka, J. Chem. Phys. **46**, 2213 (1967).

[77] R. Flesch, A. Wirsing, M. Barthel, J. Plenge, and E. Rühl, J. Chem. Phys. **128**, 074307 (2008).

[78] X. Y. Han, X. Gao, D. L. Zeng, R. Jin, J. Yan, and J. M. Li, Phys. Rev. A **89**, 042514 (2014).

[79] P. Jönsson, X. He, C. Froese Fischer, and I. P. Grant, Comput. Phys. Commun. **177**, 597 (2007).